Engineering Transactions, **73**(4): 591–615, 2025, https://doi.org/10.24423/engtrans.3593.2025
Institute of Fundamental Technological Research Polish Academy of Sciences (IPPT PAN)
Université de Lorraine • Poznan University of Technology

Research Paper

Performance of a Hybrid Ichthyoid-Waterjet Articulated Propulsor

Tomasz SZMIDT

Institute of Fundamental Technological Research, Polish Academy of Sciences
Warsaw, Poland; e-mail: tszmidt@ippt.pan.pl

The concept of a bioinspired ichthyoid-waterjet propulsor for autonomous underwater vehicles (AUVs) is investigated. The propulsor consists of an articulated fluid-conveying pipe with a propulsive fin at the end. Water drawn into the hull is accelerated to a supercritical velocity, which yields flutter vibrations of the propulsor resembling the motion of a swimming fish. The fin acts on the surrounding water and generates thrust. At the same time, the ejected water produces recoil. Using the proposed dynamical model, three types of propulsors for different swimming speeds are investigated. At low swimming speeds, the propulsive force generated by the propulsors can be up to 30% higher than the thrust of a conventional waterjet propulsor with the same physical parameters. However, this advantage in the generated thrust decreases with the swimming speed increase. The results are obtained by analyzing the approximation of the bifurcating solution and numerical simulations of the differential equation governing the dynamics.

Keywords: autonomous underwater vehicle; waterjet propulsion; fish swimming; flutter; fluid-conveying pipe.

1. Introduction

Autonomous underwater vehicles (AUVs) have a number of applications, for example, exploration and research of oceans (collecting samples, measuring currents or temperatures, creating seafloor maps, and discovering new species), inspection of pipelines and installations, mine countermeasures, and reconnaissance. From the standpoint of their propulsion, the most common are torpedo-shaped, axisymmetric vehicles driven by a fixed or vectorial propeller placed at the rear, which gives them high efficiency in forward swimming [28, 46]. Another class comprises AUV gliders, which utilize small changes in their buoyancy, combined with wings, to convert vertical motion into horizontal travel [33]. For gliders, their low power consumption enables a wide range travel and extended operation time.

Conventional, propeller-based vehicles face several limitations related to their efficiency, mechanical robustness, maneuverability, and stealth abilities. The Froude efficiency of a conventional screw propeller typically ranges between 40% and 50% (some researches claim values below 70%), while the swimming efficiency of fish and marine mammals performing body and caudal fin motion is over 80% [9, 14, 44]. As a result, devices that mimic the swimming of fish and other marine animals have been constructed and tested [15, 18]. For example, UC-Ika 2, a tuna-inspired robotic fish, demonstrated a Froude efficiency of 89%, which confirms its optimal swimming performance during cruising [27].

We are especially interested in robots that imitate marine animals propelled by body and caudal fin motions. These animals present a variety of swimming modes [35, 43]. On one side, there are anguilliform swimmers, such as eels, lampreys, or rays, whose entire body performs large-amplitude undulations in the form of a traveling wave that propagates from head to tail. Examples of robots operating in this mode are provided in [2, 38]. At the opposite side, there are thunniform swimmers, such as tuna, mackerel, shark, or dolphin, which generate propulsive force by oscillations of a rigid caudal fin of lunate shape, at the same time keeping the anterior part of the body stiff, which was experimentally verified in [1, 19]. Anguilliform locomotion mode ensures the best maneuverability (including backward swimming), while thunniform motion is the most efficient one [35]. In the middle of the spectrum of undulatory swimmers, fish such as trout or pike are located. They present the so-called (sub-)carangiform swimming mode, in which body undulations form a wave of amplitude limited in the anterior part of the body, which increases in size near the relatively stiff caudal fin, making the posterior section dominant in thrust generation. This swimming mode is the most frequently employed in underwater biomimetic robots, see [5, 26, 45].

An interesting concept combining waterjet propulsion with undulations that imitate the movement of a fish body emerged in the 1970s. It was noticed that the movement of a swimming fish's body is similar to the bending vibrations of a pipe conveying fluid and undergoing the flutter phenomenon. In such a pipe, sufficiently high internal flow velocity can lead to loss of stability of the central position and the onset of self-excited vibrations. If a flexible propulsive fin is attached along the pipe, flutter can generate additional thrust. Vibrations of the pipe result in deviations of the jet force vector from the average direction of motion and, consequently, a decrease in effective thrust. However, the additional thrust generated by the fin more than compensates for this loss, which was theoretically and experimentally confirmed in [30]. This work also highlighted the advantages of the propulsor, including quiet operation (with no propeller trace detectable by sonars) and resistance to water pollution.

Note that the ichthyoid component of the hybrid propulsor justifies quiet operation as a key motivating factor for the proposed concept. The propulsive fin's movements are silent – this is one of the primary reasons for the development of bioinspired AUVs [16, 18]. Waterjet propulsion itself generates lower noise than conventional screw propellers, primarily at high swimming speeds, where adverse phenomena such as vibrations and cavitation occur in the latter [6, 17, 24].

Research on this hydroelastic ichthyoid propulsor was resumed three decades later [10–12, 37]. In all of these studies, the hydrodynamic forces generated by the elastic propulsive fin were quantified using the the theory of anguilliform swimming mode. In [12], control of the (overcritical) internal flow velocity was implemented, enabling rapid turning maneuvers thanks to the elasticity of the tail. This control exploited both the appropriate directed of the fluid jet ejected from the pipe as well as the external surface of the propulsive fin to steer the incoming water.

In [40], a modification of the above concept was proposed. Instead of an elastic pipe, two rigid tubes connected by a viscoelastic joint were investigated. A rigid propulsive fin attached at the free end was used instead of the flexible one that extended over the entire length of the propulsor. A dynamical model of this two-degree-of-freedom system was proposed, which is simpler in analysis than the continuous model considered in the research mentioned above. It employs the Benjamin model of the dynamics of an articulated fluid-conveying pipe [3, 4] and the Lighthill elongated body theory, which quantifies the hydrodynamic forces generated by fish exhibiting (sub-)carangiform swimming. The model was used to show that the behavior of the proposed propulsor can be diverse. Both static (buckling) and dynamic (flutter) losses of stability are possible. In the latter case, we can deal with either a dangerous subcritical Hopf bifurcation, leading to a catastrophic increase in amplitude, or a desirable supercritical bifurcation resulting in a gentle onset of the vibration amplitude until reaching an orbitally stable limit cycle during which the propulsor generates a positive value of the mean thrust.

The research [40] proves that the proposed system can operate in the desired manner, i.e., performing a stable limit cycle during which the propulsive fin generates positive thrust. However, it does not verify the applicability of the concept. Most importantly, it remains unknown whether the additional thrust generated by the propulsive fin compensates for the loss of a part of the effective jet thrust resulting from the propulsor's undulations and its deviations from the average direction of motion. Solving this problem is the goal of the present work. The study examines the same system and uses the same dynamical equations as in [40]. However, in addition to the propulsive force generated by the fin, the thrust resulting from the recoil of the fluid ejected from the second pipe is

taken into account. The sum of these two thrust sources allows one to assess whether the proposed concept performs better than a conventional waterjet propulsor with the same parameters, in which jet reaction is the only source of the generated thrust. To show this, various sets of parameters are selected. Three types of propulsors are presented, distinguished by a different swimming speed at which they can operate. The vibrations and operational performance of these propulsors are characterized.

2. Investigated system

The studied system consists of two rigid pipes of lengths l_1 and l_2 ($l_1+l_2=l$) and masses m_1 and m_2 per unit length, connected by a viscoelastic joint of stiffness k_2 and damping coefficient c_2 (Fig. 1a). A triangular propulsive fin of length l_f ($0 < l_f < l_2$), span s_0, and mass M is attached at the free end perpendicularly to the plane of the tail's vibration $y = y' = 0$ (Fig. 1b). The propulsor is attached to the hull of an AUV via another joint characterized by parameters k_1 and c_1. The dynamics of AUV are disregarded in the model; instead, we consider a body of a large mass that moves at a constant speed V, for which generated thrust and the drag force are equal and opposite.

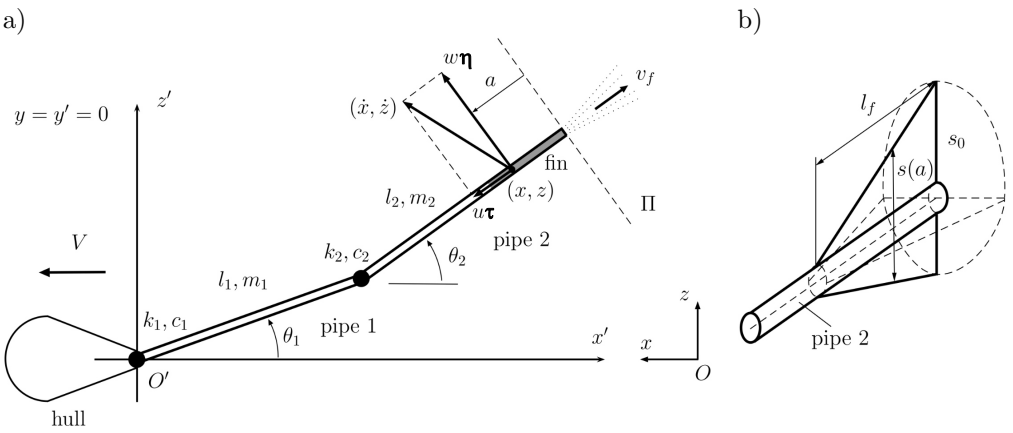

Fig. 1. Schematic of the investigated system: a) top view of the AUV with the articulated propulsor, b) propulsive fin.

Water is drawn into the hull, accelerated, and pumped through the articulated pipe at a constant velocity $v_f > V$. When the flow velocity exceeds a critical value, the central equilibrium position of the propulsor becomes unstable. If the system is subjected to dynamic loss of stability, flutter vibrations arise, and the fin accelerates the surrounding water, and thus generates propulsive force. Note that propulsion also occurs in the absence of the tail vibrations,

which is the effect of the change in momentum of the water accelerated in the system from V to v_f.

The swimming direction is along the positive x-axis of a fixed reference frame $Oxyz$. The dynamics of the propulsor are described in the inertial reference frame $O'x'y'z'$ fixed at the first joint. The straight equilibrium position of the propulsor coincides with the x'-axis. The transformation between these two frames is given as:

$$x(t) = Vt - x'(t), \qquad z(t) = z'(t), \qquad y(t) = y'(t) = 0.$$

2.1. Hydrodynamic forces generated by the fin

It is assumed that the considered propulsor mimics the undulatory motion of fishes exhibiting the (sub-)carangiform mode of locomotion. The Reynolds number associated with swimming fishes and other marine vertebrates is at least of order 10^3 [43]. For this reason, reactive forces resulting from a change in the momentum of water due to swimming motions dominate over the viscous forces, so the latter can be neglected. Lighthill proposed a theory explaining how to calculate the thrust and side forces generated by a (sub)-carangiform fish [21, 23]. This theory is applied in the present work; thus, the following assumptions regarding the AUV with the proposed propulsor are needed:

1) the propulsive fin is flat, i.e., its lateral cross-section is short in the direction of the tail's motion,
2) the propulsive fin is of a triangle shape, with the angle at the apex directed forward and below 60°,
3) the propulsor is slender in front of the fin, the height of the hull around its mass center is prominent, and it varies gradually,
4) the water momentum near each segment of the fin is perpendicular to the centerline, and it is equal to the product of the attached (virtual) water mass multiplied by the fin's velocity component in that direction,
5) the thrust is obtained by considering the changes in water momentum within the volume bounded by plane, which in every instant is perpendicular to the trailing edge of the fin.

The propulsor's position is determined by the angles $\theta_1 = \theta_1(t)$ and $\theta_2 = \theta_2(t)$, which are the angles between its segments and the horizontal axis. A curvilinear coordinate $a \in [0, l_f]$ is introduced to determine each point on the fin by their distance from the trailing edge (Fig. 1a).

The vibrating fin accelerates a volume of the surrounding water, known as the virtual (or added) mass, which generates a reactive hydrodynamic force due to inertia of the fluid. The virtual mass of water, per unit length, can be approximated by $m(a) = \frac{1}{4}\pi\rho s(a)^2$, where ρ is the density of water and $s(a)$ is

the span of the fin at a distance a from the end of the propulsor [22]. Thus, the whole mass of water accelerated by the fin is enclosed in the cone obtained by rotating the fin around its centerline (Fig. 1b).

The components of the hydrodynamic force acting in the x- and y-directions are called the thrust and side force, and are denoted by P and Q, respectively. Let us select a point $(x(a,t), z(a,t))$ on the fin. This point moves due to propulsor's vibrations and the forward translation of the system at speed V. Thus, for $a \in [0, l_f]$ its position is given by:

$$\begin{aligned} x(a,t) &= Vt - l_1 \cos\theta_1 - (l_2 - a)\cos\theta_2, \\ z(a,t) &= l_1 \sin\theta_1 + (l_2 - a)\sin\theta_2. \end{aligned} \tag{2.1}$$

The velocity vector of such a point can be written as the sum of two components – the tangential and the normal one to the fin. To do this, we introduce the unit tangent $\boldsymbol{\tau}$ and the unit normal $\boldsymbol{\eta}$ vectors:

$$\begin{aligned} \boldsymbol{\tau} &= \left(\frac{\partial x}{\partial a}, \frac{\partial z}{\partial a} \right) = (\cos\theta_2, -\sin\theta_2)\,, \\ \boldsymbol{\eta} &= \left(-\frac{\partial z}{\partial a}, \frac{\partial x}{\partial a} \right) = (\sin\theta_2, \cos\theta_2)\,. \end{aligned}$$

Then $\left(\frac{\partial x}{\partial t}, \frac{\partial z}{\partial t}\right) = u\boldsymbol{\tau} + w\boldsymbol{\eta}$, where u and w are given by scalar products of the velocity vector $\left(\frac{\partial x}{\partial t}, \frac{\partial z}{\partial t}\right)$ and the vectors $\boldsymbol{\tau}$ and $\boldsymbol{\eta}$, respectively:

$$u = \frac{\partial x}{\partial t}\frac{\partial x}{\partial a} + \frac{\partial z}{\partial t}\frac{\partial z}{\partial a}, \qquad w = \frac{\partial z}{\partial t}\frac{\partial x}{\partial a} - \frac{\partial x}{\partial t}\frac{\partial z}{\partial a}. \tag{2.2}$$

Using Eq. (2.1) the tangential and normal components of the fin's velocity at point a can be expressed by the state of the propulsor given by θ_1, θ_2 at time moment t.

The rate of change of momentum of the whole water mass accelerated by the fin is equal to the negative of the reactive force (P, Q). Because calculating the rate of change of momentum in the wake (the vortices left behind the swimming body) is difficult, Lighthill proposed studying a part of the affected fluid volume excluding the wake, i.e., the region to the left of the plane Π, which is perpendicular to the trailing edge of the fin (Fig. 1a). According to the elongated body theory, the virtual mass of water is affected mainly by w-motions of the tail, so the momentum of the considered volume equals the integral of vector $mw\boldsymbol{\eta}$ over the propulsive fin. Its time derivative can be expressed as the sum of three components: (1) the rate of change due to convection of momentum across Π, which results from the forward translation of the system; (2) the rate of change

due to the pressure acting through Π; and (3) the negative of the reactive force (P, Q) exerted by the fluid on the fin:

$$\frac{\mathrm{d}}{\mathrm{d}t}\int_0^{l_f} mw\boldsymbol{\eta}\,\mathrm{d}a = \Big[-umw\boldsymbol{\eta} + \frac{1}{2}mw^2\boldsymbol{\tau}\Big]_{a=0} - (P,Q).$$

From the aforementioned equation, we obtain the explicit formulas for the thrust and the side force generated by the propulsor:

$$\begin{aligned}
P(t) = m_0\Bigg\{&\Big[l_1\dot\theta_1\cos(\theta_1-\theta_2) + l_2\dot\theta_2 + V\sin\theta_2\Big]\\
&\cdot\Big[l_1\dot\theta_1\cos\theta_1 + \frac{l_2}{2}\dot\theta_2\cos\theta_2 - \frac{l_1}{2}\dot\theta_1\cos(\theta_1-\theta_2)\cos\theta_2 - \frac{1}{2}V\sin\theta_2\cos\theta_2\Big]\\
&- \frac{1}{3}l_f\Big[l_1\ddot\theta_1\cos(\theta_1-\theta_2)\sin\theta_2 + l_2\ddot\theta_2\sin\theta_2\\
&- l_1\dot\theta_1(\dot\theta_1-\dot\theta_2)\sin(\theta_1-\theta_2)\sin\theta_2 + l_1\dot\theta_1\dot\theta_2\cos(\theta_1-\theta_2)\cos\theta_2\\
&+ l_2\dot\theta_2^2\cos\theta_2 + V\dot\theta_2\sin 2\theta_2\Big] + \frac{1}{12}l_f^2\Big[\ddot\theta_2\sin\theta_2 + \dot\theta_2^2\cos\theta_2\Big]\Bigg\},\\
Q(t) = -m_0\Bigg\{&\Big[l_1\dot\theta_1\cos(\theta_1-\theta_2) + l_2\dot\theta_2 + V\sin\theta_2\Big]\\
&\cdot\Big[l_1\dot\theta_1\sin\theta_1 + \frac{l_2}{2}\dot\theta_2\sin\theta_2 - \frac{l_1}{2}\dot\theta_1\cos(\theta_1-\theta_2)\sin\theta_2 + V\Big(1-\frac{1}{2}\sin^2\theta_2\Big)\Big]\\
&+ \frac{1}{3}l_f\Big[l_1\ddot\theta_1\cos(\theta_1-\theta_2)\cos\theta_2 + l_2\ddot\theta_2\cos\theta_2\\
&- l_1\dot\theta_1(\dot\theta_1-\dot\theta_2)\sin(\theta_1-\theta_2)\cos\theta_2 - l_1\dot\theta_1\dot\theta_2\cos(\theta_1-\theta_2)\sin\theta_2\\
&- l_2\dot\theta_2^2\sin\theta_2 + V\dot\theta_2\cos 2\theta_2\Big] - \frac{1}{12}l_f^2\Big[\ddot\theta_2\cos\theta_2 - \dot\theta_2^2\sin\theta_2\Big]\Bigg\}.
\end{aligned} \tag{2.3}$$

These strongly nonlinear expressions determine the complex dynamics of the system for internal flows near the critical value.

2.2. Equations governing the propulsor's dynamics

Assume that the propulsor performs moderate oscillations about its central equilibrium position. Therefore, the linear Benjamin model, describing the dynamics of an articulated fluid-conveying pipe, is valid [3, 4]. The position of

the system is entirely determined by the angles θ_1 and θ_2, which describe the orientation between two rigid pipes and the x'-axis. The water inside the pipe has a mass m_f per unit length, and its flow velocity is constantly equal to v_f over the entire cross-section of the propulsor. The propulsive fin is short, so its rotational moment of inertia can be neglected, and its mass is introduced in a lumped form. According to the Lighthill theory, the hydrodynamic forces generated by the fin are mainly concentrated near its trailing edge, so we assume that they act directly at the free end of the pipe. The influence of the viscosity of the surrounding water and the drag exerted on the tubes are neglected. The following second-order ordinary differential equation (ODE) for the vector of angles $\boldsymbol{\theta} = [\theta_1, \theta_2]^{\mathrm{T}}$ is derived by analyzing the dynamic equilibrium of the system (see [40] for details):

$$\mathbf{M}(\boldsymbol{\theta})\ddot{\boldsymbol{\theta}} + \mathbf{C}\dot{\boldsymbol{\theta}} + \mathbf{K}\boldsymbol{\theta} + \mathbf{F}(\boldsymbol{\theta}, \dot{\boldsymbol{\theta}}) = \mathbf{0}, \tag{2.4}$$

where

$$\mathbf{M}(\boldsymbol{\theta}) = [m_{i,j}]_{2\times 2}\,,$$

$$m_{11} = (m_1 + m_f)\frac{l_1^3}{3} + (m_2 + m_f)l_1^2 l_2 + Ml_1^2 + m_0 l_f \frac{l_1^2}{3}\cos(\theta_1 - \theta_2)\cos\theta_2,$$

$$m_{12} = (m_2 + m_f)\frac{l_1 l_2^2}{2} + Ml_1 l_2 + m_0 l_f \frac{l_1 l_2}{3}\cos\theta_2 - m_0 l_f^2 \frac{l_1}{12}\cos\theta_2,$$

$$m_{21} = (m_2 + m_f)\frac{l_1 l_2^2}{2} + Ml_1 l_2 + m_0 l_f \frac{l_1 l_2}{3}\cos(\theta_1 - \theta_2)\cos\theta_2 + m_0 l_f \frac{l_1 l_2}{3}\theta_2 \cos(\theta_1 - \theta_2)\sin\theta_2,$$

$$m_{22} = (m_2 + m_f)\frac{l_2^3}{3} + Ml_2^2 + m_0 l_f \frac{l_2^2}{3}\cos\theta_2 - m_0 l_f^2 \frac{l_2}{12}\cos\theta_2 + m_0 l_f \frac{l_2^2}{3}\theta_2 \sin\theta_2 - m_0 l_f^2 \frac{l_2}{12}\theta_2 \sin\theta_2,$$

$$\mathbf{C} = \begin{bmatrix} m_f v_f l_1^2 + c_1 + c_2, & 2m_f v_f l_1 l_2 - c_2 \\ -c_2, & m_f v_f l_2^2 + c_2 \end{bmatrix},$$

$$\mathbf{K} = \begin{bmatrix} -m_f v_f^2 l_1 + k_1 + k_2, & m_f v_f^2 l_1 - k_2 \\ -k_2, & k_2 \end{bmatrix},$$

and

$$\mathbf{F}(\boldsymbol{\theta}, \dot{\boldsymbol{\theta}}) = [F_1, F_2]^{\mathrm{T}}\,,$$

$$F_1 = m_0 l_1 \Bigg\{ \Bigg[l_1\dot\theta_1 \cos(\theta_1-\theta_2) + l_2\dot\theta_2 + V\sin\theta_2 \Bigg] \cdot \Bigg[l_1\dot\theta_1 \sin\theta_1 + \frac{1}{2} l_2\dot\theta_2 \sin\theta_2 - \frac{1}{2} l_1\dot\theta_1 \cos(\theta_1-\theta_2)\sin\theta_2 + V\Bigg(1-\frac{1}{2}\sin^2\theta_2\Bigg)\Bigg] + \frac{1}{3} l_f \Bigg[- l_1\dot\theta_1(\dot\theta_1-\dot\theta_2)\sin(\theta_1-\theta_2)\cos\theta_2 - l_1\dot\theta_1\dot\theta_2\cos(\theta_1-\theta_2)\sin\theta_2 - l_2\dot\theta_2^2\sin\theta_2 + V\dot\theta_2\cos 2\theta_2 \Bigg] + \frac{1}{12} l_f^2 \dot\theta_2^2 \sin\theta_2 \Bigg\},$$

$$F_2 = \frac{l_2}{l_1} F_1 - m_0 l_2 \theta_2 \Bigg\{ \Bigg[l_1\dot\theta_1 \cos(\theta_1-\theta_2) + l_2\dot\theta_2 + V\sin\theta_2 \Bigg] \cdot \Bigg[l_1\dot\theta_1 \cos\theta_1 + \frac{1}{2} l_2\dot\theta_2 \cos\theta_2 - \frac{1}{2} l_1\dot\theta_1 \cos(\theta_1-\theta_2)\cos\theta_2 - \frac{1}{2} V\sin\theta_2\cos\theta_2 \Bigg] - \frac{1}{3} l_f \Bigg[- l_1\dot\theta_1(\dot\theta_1-\dot\theta_2)\sin(\theta_1-\theta_2)\sin\theta_2 + l_1\dot\theta_1\dot\theta_2\cos(\theta_1-\theta_2)\cos\theta_2 + l_2\dot\theta_2^2\cos\theta_2 + V\dot\theta_2\sin 2\theta_2 \Bigg] + \frac{1}{12} l_f^2 \dot\theta_2^2 \cos\theta_2 \Bigg\}.$$

Let us substitute $u_1 = \theta_1$, $u_2 = \theta_2$, $u_3 = \dot\theta_1$, $u_4 = \dot\theta_2$, and denote $\mathbf{u} = [u_1, u_2, u_3, u_4]^{\mathrm{T}}$. Then, we can transform the second-order ODE given in Eq. (2.4) into a set of four first-order nonlinear differential equations in explicit form:

$$\dot{\mathbf{u}} = \mathbf{f}(\mathbf{u}; v_f), \qquad \mathbf{f} = [f_1, f_2, f_3, f_4]^{\mathrm{T}}. \tag{2.5}$$

3. Approximate and numerical solution

The trivial equilibrium is a steady state of Eq. (2.5), i.e., $\mathbf{f}(\mathbf{0}, v_f) = \mathbf{0}$ for all v_f. The flow velocity is a bifurcation parameter; when it reaches a critical value $v_f^{(0)}$, a new type of solution appears in the close proximity of the steady equilibrium. Let $\mathbf{L}(v_f) = \left[\frac{\partial f_i}{\partial u_j}(\mathbf{0}; v_f)\right]_{4\times 4}$ be the matrix of Eq. (2.5) linearized at $\mathbf{u} = \mathbf{0}$ and $r_1(v_f) = a(v_f) + \mathrm{i}b(v_f)$, $b(v_f) \geq 0$ – one of the pair of complex conjugate eigenvalues of $\mathbf{L}$ with the largest real part, called the decisive eigenvalue. For $v_f < v_f^{(0)}$, all eigenvalues of $\mathbf{L}(v_f)$ have negative real parts, so the trivial equilibrium of the propulsor is asymptotically stable. As the flow velocity increases, the decisive eigenvalues cross the imaginary axis which happens at $v_f = v_f^{(0)}$, i.e., $a(v_f^{(0)}) = 0$. We are interested in the case when $b(v_f^{(0)}) = \Omega^{(0)} > 0$, which leads to a dynamic type of instability (Hopf bifurcation)[1)]. In this case,

[1)] The propulsor buckles if the decisive eigenvalues become equal and cross the imaginary axis along the real axis.

self-excited flutter vibrations with an initial frequency $\Omega^{(0)}$ arise, which enables the propulsor to vibrate similarly to a swimming fish motion.

To investigate the near-critical behavior of the propulsor, an analytical approximation of the bifurcating periodic solution is constructed using the method of Iooss and Joseph [13], see [40, 41] for derivation details. Let $\langle \mathbf{a}, \mathbf{b} \rangle = \sum a_i \overline{b}_i$ be the scalar product in $\mathbb{C}^4$ and denote by $\mathbf{f_u} = \left[f_{u,1}, ..., f_{u,4}\right]^{\mathrm{T}}$, $\mathbf{f_{uu}} = \left[f_{uu,1}, ..., f_{uu,4}\right]^{\mathrm{T}}$, and $\mathbf{f_{uuu}} = \left[f_{uuu,1}, ..., f_{uuu,4}\right]^{\mathrm{T}}$ the following multilinear operators:

$$f_{u,i}\left(\mathbf{a}\right) = \sum_{k=1}^{4} \frac{\partial f_i}{\partial u_k}\bigg|_{v_f = v_f^{(0)},\, \mathbf{u}=\mathbf{0}} a_k,$$

$$f_{uu,i}\left(\mathbf{a}|\mathbf{b}\right) = \sum_{k=1}^{4}\sum_{l=1}^{4} \frac{\partial^2 f_i}{\partial u_k \partial u_l}\bigg|_{v = v_f^{(0)},\, \mathbf{u}=\mathbf{0}} a_k b_l,$$

$$f_{uuu,i}\left(\mathbf{a}|\mathbf{b}|\mathbf{c}\right) = \sum_{k=1}^{4}\sum_{l=1}^{4}\sum_{m=1}^{4} \frac{\partial^3 f_i}{\partial u_k \partial u_l \partial u_m}\bigg|_{v = v_f^{(0)},\, \mathbf{u}=\mathbf{0}} a_k b_l c_m,$$

where

$$\mathbf{a}, \mathbf{b}, \mathbf{c} \in \mathbb{C}^4, \qquad i = 1, ..., 4.$$

Then the first (harmonic) approximation is given by:

$$u_i = 2\sqrt{2\frac{v_f - v_f^{(0)}}{v_f^{(2)}}}\,|q_i| \cos\left(\Omega t + \arg q_i\right), \qquad i = 1, ..., 4,$$

$$\Omega = \Omega^{(0)} + \Omega^{(2)} \frac{v_f - v_f^{(0)}}{v_f^{(2)}},$$

$$v_f^{(2)} = -\frac{\mathrm{Re}\left(R_2\right)}{3\frac{\mathrm{d}a(v_f^{(0)})}{\mathrm{d}\,v_f}}, \qquad \Omega^{(2)} = v_f^{(2)} \frac{\mathrm{d}\,b(v_f^{(0)})}{\mathrm{d}\,v_f} + \frac{1}{3}\mathrm{Im}\left(R_2\right),$$

$$R_2 = 3\left\langle \mathbf{f_{uu}}\left(\mathbf{q}|\mathbf{k}\right) + \mathbf{f_{uu}}\left(\overline{\mathbf{q}}|\mathbf{l}\right) + \mathbf{f_{uuu}}\left(\mathbf{q}|\mathbf{q}|\overline{\mathbf{q}}\right), \mathbf{q}^{\star}\right\rangle, \tag{3.1}$$

$$\left[\mathbf{L}(v_f^{(0)}) - r_1(v_f^{(0)})\mathbf{I}\right]\mathbf{q} = \mathbf{0},$$

$$\left[\mathbf{L}^{\mathrm{T}}(v_f^{(0)}) - \overline{r}_1(v_f^{(0)})\mathbf{I}\right]\mathbf{q}^{\star} = \mathbf{0}, \qquad \langle \mathbf{q}, \mathbf{q}^{\star}\rangle = 1,$$

$$\mathbf{L}(v_f^{(0)})\mathbf{k} = -2\mathbf{f_{uu}}(\mathbf{q}|\overline{\mathbf{q}}),$$

$$\left[\mathbf{L}(v_f^{(0)}) - 2\mathrm{i}\Omega^{(0)}\mathbf{I}\right]\mathbf{l} = -\mathbf{f_{uu}}(\mathbf{q}|\mathbf{q}),$$

$$v_f^{(2)} > 0 \Rightarrow v_f > v_f^{(0)}, \qquad v_f^{(2)} < 0 \Rightarrow v_f < v_f^{(0)}.$$

If $v_f^{(2)} > 0$, the bifurcation is supercritical, which means that for $v_f < v_f^{(0)}$ the zero equilibrium is globally stable and when the internal flow increases beyond the critical value, the amplitude of flutter gradually increases. If $v_f^{(2)} < 0$, the bifurcation is subcritical, for $v_f < v_f^{(0)}$ the trivial equilibrium is locally stable – for sufficiently large initial deflection the system may exhibit an abrupt, even catastrophic, growth of the flutter amplitude. We are interested in the first type of the Hopf bifurcation only, as it ensures the safe operation of the propulsor.

The approximate solution is used to analyze the dynamics of the propulsor, the average thrust it produces, and its propulsive performance. Moreover, numerical simulations of Eq. (2.5) with the Fehlberg–Runge–Kutta fourth-fifth (RKF45) method implemented in Maple software are performed to support the obtained results.

4. Propulsors for various swimming speeds

4.1. Physical parameters

Propulsors of three types, which enable reaching various swimming speeds, are going to be investigated: low-speed propulsor ($V \leq V_{\max} = 0.05$ m/s), intermediate ($V_{\max} = 0.50$ m/s), and high-speed ($V_{\max} = 1.03$ m/s). For swimming speeds higher than $V_{\max}$, the bifurcation changes its character from supercritical to subcritical, which compromises the safe operation of the system.[2)]

All three propulsors have a total length of $l_1 + l_2 = 1$ m and are constructed from rigid tubes with an internal diameter $d = 12$ mm, so the linear mass density of the conveyed fluid equals $m_f = 0.1131$ kg/m (the water density $\rho = 1000$ kg/m^3 is assumed). To enable the propulsor to perform a wavelike motion resembling the motion of a swimming fish, the mass per unit length of the second segment must be significantly smaller than that of the first one. Thus, it is assumed that $m_2 = 0.0334$ kg/m, a value obtained for a tube made from carbon fiber with a density of 1700 kg/m^3, and a 0.5 mm wall thickness. The first tube is ten times heavier ($m_1 = 0.3338$ kg/m), which can be achieved by manufacturing the tube from aluminum (or steel, brass, etc.) with an appropriately selected wall thickness.

A triangular propulsive fin with a span $s_0 = 0.12$ m and a length $l_f = 0.105$ m is attached to the end of the second tube. Then, the mass of water added at the end of the fin is $s_0 = 0.12$ kg/m. In addition, the forward apex angle is below 60°, so the Lighthill assumption of fin's slenderness is satisfied. It is assumed that the fin is made from a 1 mm thick carbon plate, which gives it mass $M = 0.0107$ kg.

[2)] In the case of the low-speed propulsor it is possible to increase the swimming speed up to $V = 0.06$ m/s; however, beyond this point the numerical solution differs significantly from the analytical approximation, which makes the analysis unreliable.

Other physical parameters vary depending on the type of propulsor and are presented in the Table 1. The most common approach to manufacturing viscoelastic joints between the pipes is to fit a short rubber tube over the adjacent two ends of the pipes, and tighten it with a wire [4, 39]. The planar motion of such a system may be imposed by constructing additional pivot joints [34]. The stiffness and damping coefficients can be determined experimentally after the system is constructed.

TABLE 1. Physical parameters of the considered propulsors of three types.

Parameter	Unit	Low-speed	Intermediate	High-speed
$l_1/(l_1+l_2)$	–	0.88	0.80	0.70
k_1	$\mathrm{N\cdot m}$	20	90	110
k_2	$\mathrm{N\cdot m}$	0.9	0.9	0.75
c_1	$\mathrm{N\cdot m\cdot s}$	0.01	0.01	0.005
c_2	$\mathrm{N\cdot m\cdot s}$	0.14	0.2	0.1

4.2. Near-critical behavior of the system

This subsection explains the behavior of the system for internal flows near the critical value, using the intermediate-type of propulsor. Figure 2 shows the amplitude of the flutter vibration as a function of internal flow velocity for the three selected swimming speeds. Continuous lines denote the amplitude from the analytical approximation given in Eq. (3.1) for vibrations of θ_1 (solid lines) and θ_2 (dashed lines), while the rhomboidal dots stand for the amplitudes of the numerical solution (solid and empty dots, respectively, for θ_1 and θ_2).

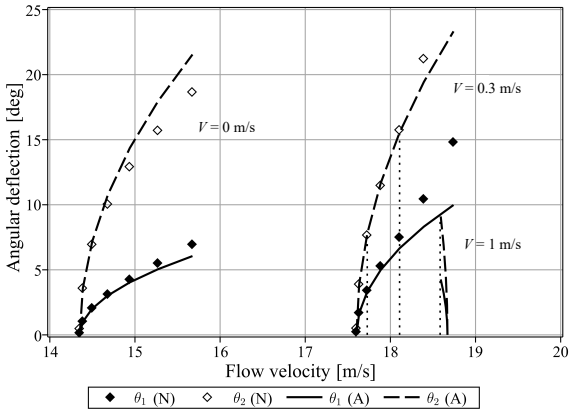

FIG. 2. Bifurcation diagram of the intermediate propulsor for swimming speeds $V = 0$ m/s, 0.3 m/s, 1 m/s, lines – analytical approximation of amplitude θ_1 (solid) and θ_2 (dashed), diamonds – amplitude values obtained numerically.

The critical flow velocity amounts to $v_f^{(0)} = 14.35$ m/s, 17.60 m/s, and 18.67 m/s, respectively, for swimming speed $V = 0$ m/s, 0.3 m/s, and 1 m/s. For $v_f < v_f^{(0)}$, the system stays in the central equilibrium position, and the propulsor generates thrust solely due to the acceleration of the fluid jet ejected in the direction opposite to the swimming direction. For $v_f > v_f^{(0)}$ the behavior depends on the swimming speed. For $V = 0$ m/s and $V = 0.3$ m/s, the self-excitation is soft, so for the internal flow velocity above the critical value, orbitally stable periodic oscillations of the propulsor appear. Then, the propulsor acts on the water through the fin and generates additional thrust. At the same time, a small part of the effective thrust of the jet is lost due to the deflection of the tip from the direction of motion. For swimming speed $V = 1$ m/s, the bifurcation is subcritical, so for flows below the critical one an unstable periodic cycle marked in the figure exists. This solution is impossible to be reproduced numerically.

The discrepancy between the analytical and numerical solutions becomes significant after reaching the vibration amplitude of about 20°, which confirms the conclusions from [40]. Such a limit also stems from the fact that the model does not include geometric non-linearities affecting the dynamics of the articulated pipe conveying fluid.

Suppose the swimming speed amounts to $V = 0.3$ m/s, so the system undergoes a supercritical bifurcation. For internal flows slightly above the critical value, the convergence of the solution to the limit cycle is slower than when the flow significantly exceeds the critical one. This is shown in Figs. 3a and 3b, which present numerically computed angular deflections of θ_1 and θ_2 for initial conditions $\theta_1(0) = 0.3°$ and $\theta_2(0) = \dot{\theta}_1(0) = \dot{\theta}_2(0) = 0$. In Fig. 3a the internal flow velocity amounts to $v_f = 17.73$ m/s (which corresponds to the third dot in Fig. 2 for $V = 0.3$ m/s), and in Fig. 3b the internal flow is higher, $v_f = 18.11$ m/s (the fifth dot in Fig. 2 for $V = 0.3$ m/s).

The last two figures refer to the case $V = 1$ m/s, where the propulsor is subjected to hard self-excitation. The solution for the subcritical flow velocity $v_f = 18.58 < v_f^{(0)} = 18.67$ m/s and the initial deflection $\theta_1(0) = 2°$ converges to zero, see Fig. 3c. However, a slight increase of the initial deflection to $\theta_1(0) = 2.5°$ causes the solution to explode and reach the amplitude of about 40°, exceeding the range of applicability of the model (Fig. 3d). The existence of this stable, large-amplitude limit cycle indicates that the curve in the bifurcation diagram for $V = 1$ m/s bends to the right at higher amplitudes. However, to prove this, it would be necessary to calculate at least a second approximation of the bifurcating solution, which would also require an appropriate extension of the model and is beyond the scope of this work.

In the next section, the performance and vibration characteristics of the propulsors will be investigated for various swimming speeds. For each type of

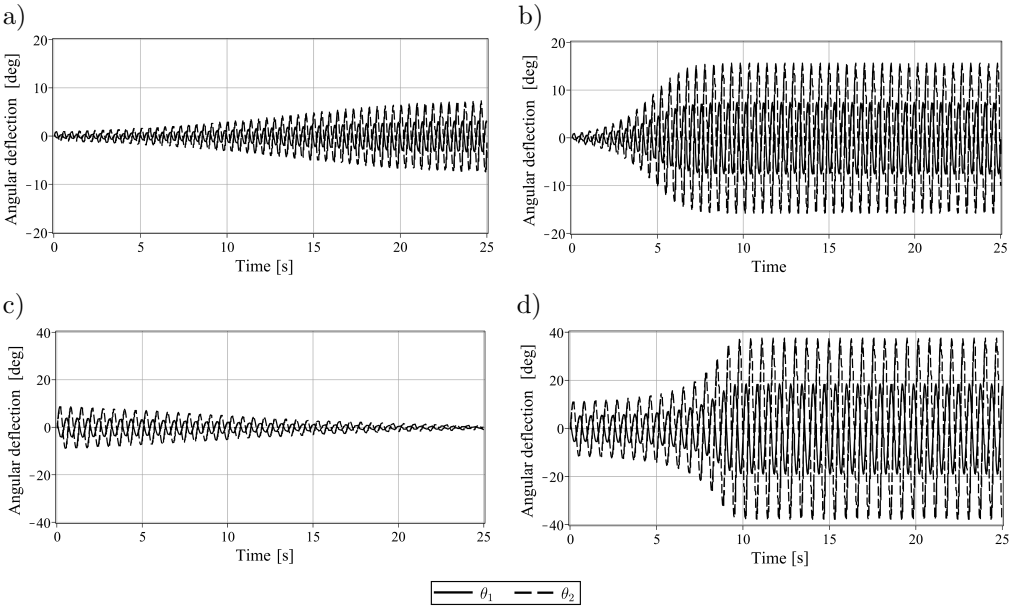

FIG. 3. Angular vibrations of θ_1 (solid lines) and θ_2 (dashed lines), for selected cases of the intermediate propulsor: a) $V = 0.3$ m/s, $v_f = 17.73$ m/s, initial deflection $\theta_1(0) = 0.3°$, b) $V = 0.3$ m/s, $v_f = 18.11$ m/s, $\theta_1(0) = 0.3°$, c) $V = 1$ m/s, $v_f = 18.58$ m/s, $\theta_1(0) = 2°$, d) $V = 1$ m/s, $v_f = 18.58$ m/s, $\theta_1(0) = 2.5°$.

the propulsor and the swimming speed $V \leq V_{\max}$, the critical flow velocity $v_f^{(0)}$ will be computed. Then, the internal flow velocity v_f at which the larger of the two angular amplitudes from the analytical approximation reaches 20° will be determined. The results for smaller amplitude are qualitatively the same but less distinct.

5. Performance of the propulsors

5.1. Ichthyoid-waterjet thrust and propulsion efficiency

The working propulsor generates thrust due to the action of the fin on the surrounding water and the jet of water flowing out of the pipe. The average value of the first component amounts to $\overline{P} = \frac{1}{T}\int_0^T P(t)\,\mathrm{d}t$, where T is the period of the propulsor's vibrations, and $P(t)$ – the instantaneous value of the thrust force given by Eq. (2.3). The average value of the waterjet thrust $\overline{J}$ results from the change in the momentum of water accelerated from the swimming speed V up to the internal flow velocity v_f, projected onto the direction of motion:

$$\overline{J} = \rho\pi\left(\frac{d}{2}\right)^2 v_f\,(v_f - V)\,\frac{1}{T}\int_0^T \cos\left(\theta_2(t)\right)\mathrm{d}t.$$

The total thrust $\overline{P}+\overline{J}$ generated by the investigated propulsor is compared to the thrust J_s produced by a straight waterjet propulsor of the same geometrical parameters ejecting water at the same velocity v_f, i.e.,

$$J_s = \rho\pi \left(\frac{d}{2}\right)^2 v_f \left(v_f - V\right).$$

This allows us to answer the question of whether the loss of part of the recoil resulting from the deflection of the second tube by the angle θ_2 from the direction of motion is compensated by the additional thrust $\overline{P}$ generated by the fin.

Figure 4 shows that the total thrust of the considered propulsors exceeds that generated by a straight waterjet propulsor across the entire range of considered swimming speeds; however, this advantage decreases with the increase of V. The greatest gain is observed for the low-speed propulsor and reaches 30%, while the lowest for the high-speed propulsor, where it equals about 1%–2% (Fig. 4b). A reasonable compromise is offered here by the intermediate propulsor, for which the gain of 5%–10% is obtained in the practically useful range of swimming speeds up to $V_{\max} = 0.5$ m/s. Let us emphasize that the analysis of the numerical solution (solid lines) leads to the same conclusions as the analysis of the analytical approximation (dashed lines).

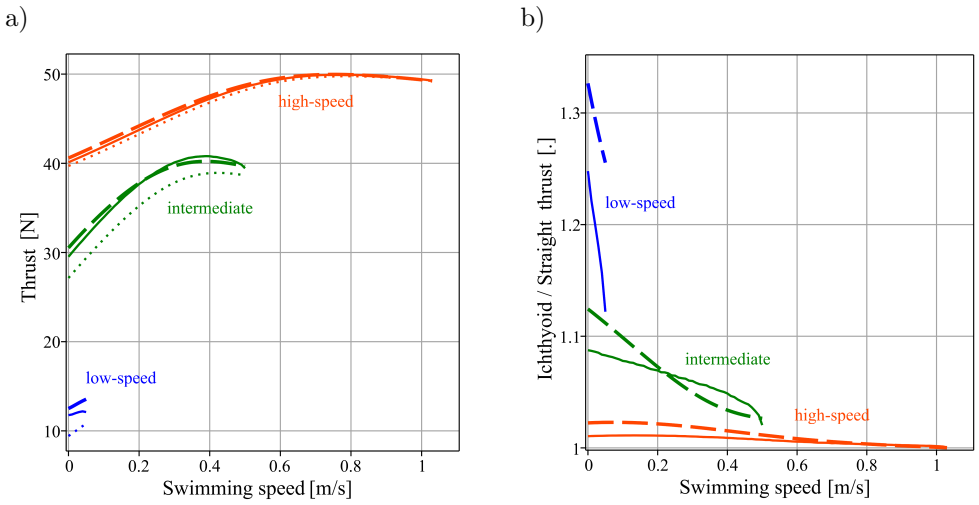

FIG. 4. a) Mean thrust generated by the investigated propulsors, b) mean thrust related to the thrust produced by straight (waterjet) propulsors with the same parameters; solid lines – numerical solution, dashed lines – analytical approximation, dotted lines – straight propulsor.

The increase in thrust generated by the propulsors in relation to the swimming speed, visible in Fig. 4a, results from the stabilizing effect of the external

flow. With increasing V, a larger internal flow v_f is required to induce a flutter of amplitude 20°. This is explained in more detail in Fig. 5, in which the solid lines denote the internal flow velocity v_f, and the dotted lines – its critical value $v_f^{(0)}$.

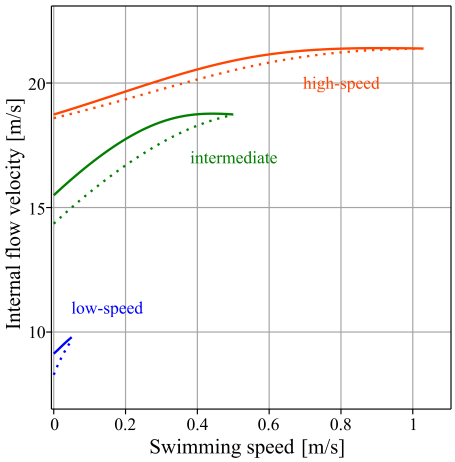

FIG. 5. Critical (dotted lines) and actual (solid lines) internal flow velocity.

Note that a small increase in flow above the critical value leads to flutter with the desired amplitude. This enables easy control of the ichthyoid thrust component but requires precise control of the internal flow velocity, especially in the case of the high-speed propulsor. It seems that the best compromise here is offered by the intermediate propulsor.

The observed high values of the internal flow velocity, 15 m/s–20 m/s, suggest a high risk of hydrodynamic cavitation. The cavitation number for the studied system is defined as [29]:

$$\sigma = \frac{p - p_v}{\frac{1}{2}\rho v_f^2},$$

where p is the ambient pressure, p_v is the vapor pressure of water, and ρ is the water density. At low swimming depths and $v_f = 21$ m/s, the cavitation number can be as low as 0.45. Thus, cavitation may appear, which leads to emission of noise and erosion of the propulsor. Various countermeasures may be taken to diminish the risk of cavitation, for example, increasing the pipe diameter to reduce the internal flow velocity. Further research on this issue is necessary.

The propulsive performance of the fish-like motion is analyzed using classical metrics: the Froude efficiency and the Strouhal number. The first one denotes the ratio of useful power (mean thrust multiplied by swimming speed) to the power

consumed to produce that thrust. The latter can be calculated by considering the kinetic energy of the water associated with w-motions of the fin, which is partially lost in the wake due to forward swimming. According to the Lighthill model [23], the average energy loss is given by:

$$\overline{E} = \frac{1}{T}\int_0^T \left[\frac{1}{2}mw^2u\right]_{a=0} \mathrm{d}t,$$

where w and u are defined in Eq. (2.2). This yields the following formula for the Froude efficiency [20, 35, 36]:

$$\eta = \frac{V\overline{P}}{V\overline{P} + \overline{E}}.$$

Figure 6a shows the Froude efficiency calculated for the considered propulsors performing self-excited vibrations with an amplitude 20°. The efficiency increases with the swimming speed and is the highest for the high-speed propulsor. However, even in this case, the efficiency hardly reaches the values estimated for real-world anguilliform and carangiform swimmers [25].

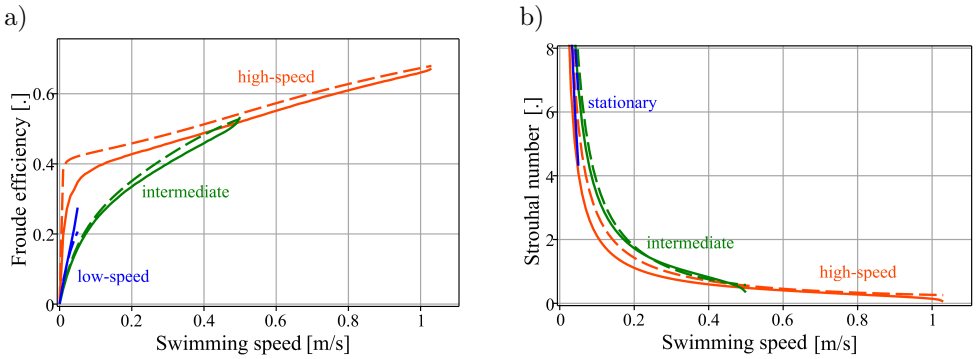

FIG. 6. a) Froude efficiency, b) Strouhal number of the propulsors; solid lines – numerical solution, dashed lines – analytical approximation.

The Strouhal number is defined as the tail beat frequency multiplied by the lateral displacement of the propulsive fin, divided by the average swimming speed [8]:

$$\mathrm{St} = \frac{2A}{TV},$$

where A is the vibration amplitude of the propulsor's free end calculated both from the analytical approximation and the numerical solution. For most marine animals propelled by body and caudal fin motion, the Strouhal number is between 0.25 and 0.35 [42]. These values can be achieved only by the high-speed propulsor at higher swimming speeds (Fig. 6b).

5.2. Amplitude, frequency and phase shift of pipe segments

The angular amplitude of the second segment's vibrations is about twice that of the first segment (Fig. 7). Let us recall that the internal flow velocity was selected so that the maximum amplitude of vibrations was 20°; for all considered propulsors and swimming speeds, this is the amplitude of the second segment.

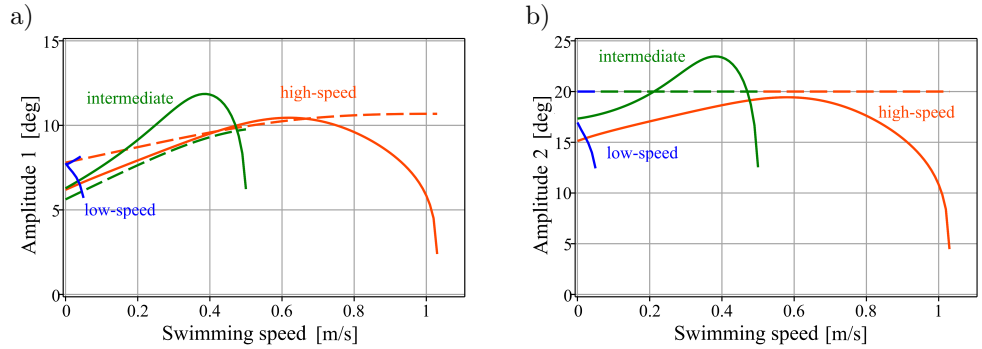

FIG. 7. Angular amplitude of (a) the first and (b) the second pipe segment; solid lines – numerical solution, dashed lines – analytical approximation.

The observed discrepancy between the amplitude obtained from Eq. (3.1) (dashed lines) and the amplitude from the numerical solution (solid lines) confirms the necessity of using both types of solutions in the analysis. The largest discrepancies can be observed near the swimming speed at which the bifurcation changes from supercritical to subcritical one. A comparison of bifurcating branches for the high-speed propulsor and swimming speeds $V = 0.6$ m/s and $V = 1$ m/s shows that discrepancies are greater in the latter case (Fig. 8).

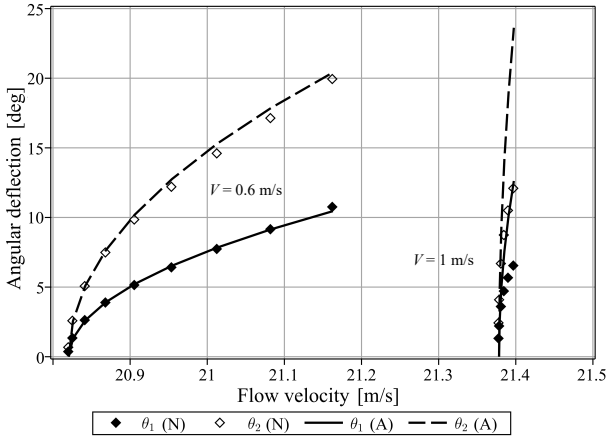

FIG. 8. Bifurcation diagram of the high-speed propulsor at swimming speeds $V = 0.6$ m/s and $V = 1$ m/s, lines – analytical approximation of amplitude θ_1 (solid) and θ_2 (dashed), diamonds – values obtained numerically.

Moreover, when the bifurcating branch is steeper, convergence of the numerical solution to the limit cycle is slower.

In the case of the propulsor's vibration frequency (Fig. 9a) and the phase shift between the pipe segments (Fig. 9b), the agreement between the numerical solution and the analytical approximation is better. The vibration frequency only slightly depends on the swimming speed – it gently decreases with the increase of V. The low-speed propulsor is characterized by the lowest vibration frequency (approx. 1 Hz), the intermediate propulsor by a frequency about twice as high, and the highest vibration frequency (∼3 Hz) is exhibited by the high-speed propulsor.

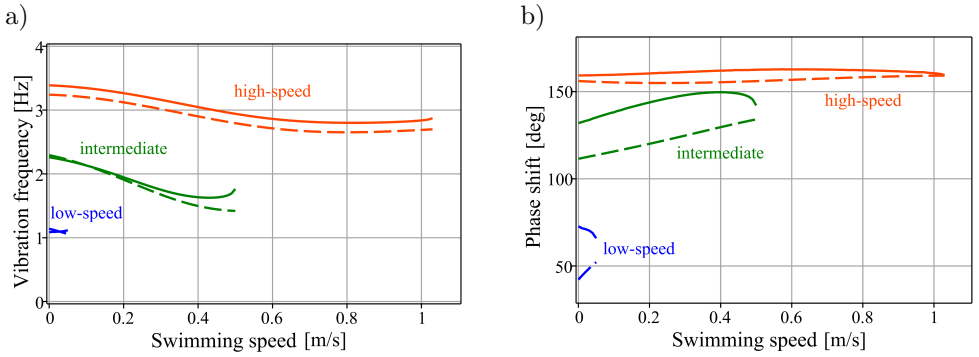

FIG. 9. a) Vibration frequency, b) angular phase shift between pipe segments; solid lines – numerical solution, dashed lines – analytical approximation.

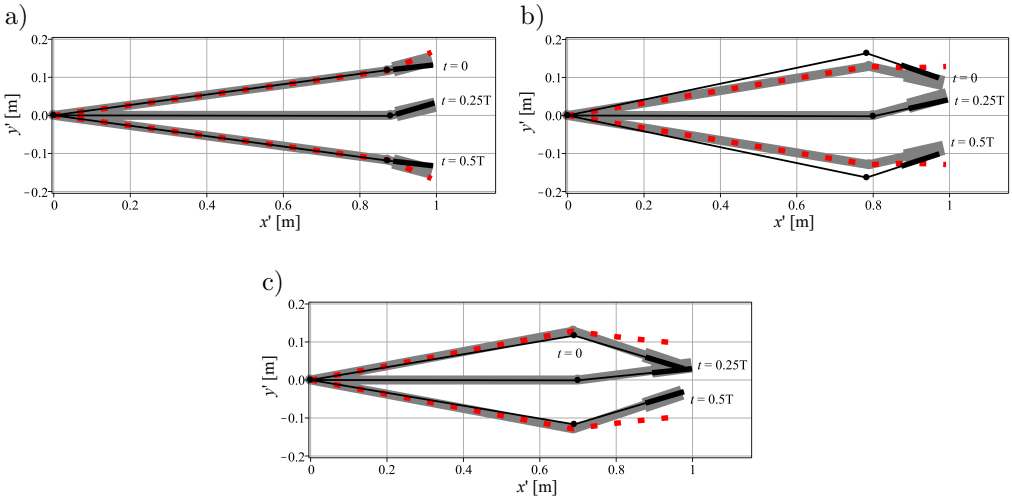

FIG. 10. Positions of (a) the low-speed, (b) the intermediate, and (c) the high-speed propulsors at selected moments within the vibration period; black lines – numerical solution, gray lines – analytical approximation, and red dots – vibration envelope of the analytical approximation.

Similarly, the dependence of the phase shift on the swimming speed is weak, but this time it is positive. The minor phase shift is characteristic of the low-speed propulsor (approx. 50°–70°), and it is larger for the intermediate one (110°–150°), while in the case of the high-speed propulsor, the fin vibrates almost in antiphase with respect to the first pipe segment (160°–170°).

Finally, let us examine the propulsors' positions throughout one vibration cycle (Fig. 10). The gray, bold lines denote positions calculated from the analytical approximation, the black lines indicate numerically determined positions, and the red dots represent the envelope of deflection from the analytical approximation. The figures show that the propulsor's motion resembles the undulating motion of a swimming fish body, especially in the case of the low-speed and intermediate propulsors, for which the envelope increases toward the free end.

6. Discussion and conclusions

The concept of a hybrid ichthyoid-waterjet propulsor excited by internal flow was investigated. The propulsor is constructed of two articulated pipes that convey fluid and are interconnected by a viscoelastic joint. A triangular propulsive fin is attached to the free end, and the entire system is connected to the hull of an AUV. The sucked-in water is accelerated to a supercritical speed, which, under certain conditions, leads to orbitally stable flutter vibrations of the propulsor. The propulsor performs motion resembling the motion of a swimming fish, and the fin acts on surrounding water to generate thrust. At the same time, the acceleration of water in the pipe produces a recoil force. Both of these thrust sources together allow for generating an average propulsive force greater than that of a simple waterjet propulsor with the same physical parameters, thereby justifying the proposed concept.

The already proposed model of the dynamics of an articulated pipe with flow, subjected to hydrodynamic forces resulting from the action of the attached propulsive fin, was used. This model allowed us to investigate vibrations of moderately high amplitude $\sim 20°$. Let us notice that the applied the Lighthill elongated body theory adequately describes the hydrodynamic forces for arbitrarily large deflections. Thus, it is worthwhile to generalize the linear Benjamin model of the dynamics of the articulated pipe with flow to account for large deflections. This is interesting because, within the considered range of amplitudes, the proposed method proved to be even more effective as the amplitude increased.

Three types of propulsors for different ranges of swimming speeds (low-speed, intermediate, and high-speed ones) were investigated. The intermediate propulsor offers the best compromise between performance and applicability. The thrust that it generates is from a few percent up to $\sim 10\%$ greater than that of a comparable conventional waterjet propulsor. This advantage is observed

at swimming speeds in the range from 0 m/s to 0.5 m/s. Thus, the potential application of this propulsor is for AUVs traveling at low speeds or those in which, after reaching a given speed, the propulsor is immobilized and operates as a conventional waterjet propulsor. In the case of the low-speed propulsor, the advantage over the reference system is significantly greater and reaches ∼30%, but it is limited to swimming speeds close to zero. In contrast, the high-speed propulsor exhibits at most a 2%–3% advantage, which is not worth the complications of designing and manufacturing.

The Froude efficiency of the intermediate propulsor is relatively low, reaching a maximum of $\eta \approx 0.5$ for a swimming speed $V = 0.5$ m/s, which is significantly lower than the values within the range from approximately 0.7 to 0.9 estimated for fish exhibiting the carangiform swimming mode [25]. This may be related to the relatively high Strouhal number of this propulsor, $\mathrm{St} \approx 0.5$ for $V = 0.5$ m/s, which is above the range $[0.25, 0.35]$ reported for living organisms [42]. Therefore, there is still a need to search for the optimal propulsor's parameters, perhaps using computational fluid dynamics (CFD) methods.

The system's behavior is highly sensitive to the selection of parameters. In particular, the three types of propulsors considered differ only in the ratio of the lengths of both pipes and in the values of the coefficients of elasticity and damping of the joints. It is a known phenomenon – critical flow velocity, the type of instability, and the near-critical behavior of pipes conveying fluid are all strongly susceptible to even small changes in the physical parameters of the system and the introduction of new effects [31, 32]. This extraordinary sensitivity to additional impacts is a feature of a broader class of non-conservative systems subjected to a follower load, of which fluid-carrying pipes are the most common example [7].

The considered model disregards effects that are less important for understanding the dynamics, such as viscosity of the medium or the fact that the value of the internal flow velocity changes during the vibration cycle. Some of the assumed parameters, such as the values of the stiffness and damping coefficients, are difficult to determine precisely in a real-world system [4]. This will make the future empirical verification of the results challenging. The test system should allow for easy modification of the stiffness and damping of the viscoelastic joints, as well as enable changes to the geometric and mass parameters of the pipes and the propulsive fin. The selection of optimal parameters and experimental verification are interesting directions for future research, mainly because the considered propulsors operate outside the optimal range of performance defined by the Froude efficiency and the Strouhal number for living fish exhibiting a (sub-)carangiform swimming mode of locomotion.

The system's susceptibility to parameter changes offers an opportunity for implementing a control strategy, for example, by changing the internal flow ve-

locity or stiffness and damping of the joints. In [12], a control scheme was implemented in a model of an AUV equipped with a flutter-excited flexible propulsor. The control of the internal flow velocity allowed for turning maneuvers. Applying this control approach to the system considered in this work requires transforming the dynamical equations into a non-inertial reference frame associated with the AUV. This is interesting also because, to the author's knowledge, there is no research on the dynamics of articulated fluid-carrying pipes vibrating in a non-inertial reference frame, even if the propulsive fin and the generated hydrodynamic forces are omitted.

Another control problem, one that does not require abandoning the assumption of constant AUV's velocity, can also be considered. The internal flow velocity or other parameters can be controlled so that, for a given range of swimming speeds, either the average value of the generated thrust is maximized or the fluctuations of the thrust are minimized. As for the latter objective, it is worth noting that the thrust generated by the fin can drop below zero, which means that the fin exerts drag, not the propulsive force [23].

Fundings

No funds or grants were received for this work.

Conflict of interest

The author declares that there are no known competing financial interests or personal relationships that could influence the work reported in this paper.

References

1. Algarín-Pinto J.A., Garza-Castañón L.E., Vargas-Martínez A., Minchala-Ávila L.I., Dynamic modeling and control of a parallel mechanism used in the propulsion system of a biomimetic underwater vehicle, *Applied Sciences*, **11**(11): 4909, 2021, https://doi.org/10.3390/app11114909.

2. Bayat B., Crespi A., Ijspeert A., Envirobot: A bio-inspired environmental monitoring platform, [in:] *2016 IEEE/OES Autonomous Underwater Vehicles (AUV)*, pp. 381–386, 2016, https://doi.org/10.1109/AUV.2016.7778700.

3. Benjamin T.B., Dynamics of a system of articulated pipes conveying fluid. I. Theory, *Proceedings of the Royal Society of London. Series A, Mathematical and Physical Sciences*, **261**(1307): 457–486, 1961, https://doi.org/10.1098/rspa.1961.0090.

4. Benjamin T.B., Dynamics of a system of articulated pipes conveying fluid. II. Experiments, *Proceedings of the Royal Society of London. Series A., Mathematical and Physical Sciences*, **261**(1307): 487–499, 1961, https://doi.org/10.1098/rspa.1961.0091.

5. Clapham R.J., Hu H., *iSplash*: Realizing fast carangiform swimming to outperform a real fish, [in:] *Robot Fish. Springer Tracts in Mechanical Engineering*, Du R., Li Z., Youcef-Toumi K., Valdivia y Alvarado P. [Eds], pp. 193–218, Springer, Berlin, Heidelberg, 2015, https://doi.org/10.1007/978-3-662-46870-8_7.

6. Ebrahimi A., Razaghian A., Seif M., Zahedi F., Nouri-Borujerdi A., A comprehensive study on noise reduction methods of marine propellers and design procedures, *Applied Acoustics*, **150**: 55–69, 2019, https://doi.org/10.1016/j.apacoust.2018.12.004.

7. Elishakoff I., Controversy associated with the so-called "follower forces": Critical overview, *Applied Mechanics Reviews*, **58**(2): 117–142, 2005, https://doi.org/10.1115/1.1849170.

8. Fish F., Lauder G., Not just going with the flow, *American Scientist*, **101**(2): 114–123, 2013, https://bpb-us-e1.wpmucdn.com/sites.harvard.edu/dist/6/58/files/2022/03/Fish.Lauder.2013.pdf.

9. Fish F.E., Advantages of natural propulsive systems, *Marine Technology Society Journal*, **47**(5): 37–44, 2013, https://doi.org/10.4031/MTSJ.47.5.2.

10. Hellum A., Mukherjee R., Bénard A., Hull A.J., Modeling and simulation of the dynamics of a submersible propelled by a fluttering fluid-conveying tail, *Journal of Fluids and Structures*, **36**: 83–110, 2013, https://doi.org/10.1016/j.jfluidstructs.2012.08.006.

11. Hellum A., Mukherjee R., Hull A.J., Flutter instability of a fluid-conveying fluid-immersed pipe affixed to a rigid body, *Journal of Fluids and Structures*, **27**(7): 1086–1096, 2011, https://doi.org/10.1016/j.jfluidstructs.2011.03.002.

12. Hellum A.M., Strefling P.C., Mukherjee R., Maneuvering and control of a synergistically propelled ichthyoid, [in:] *Proceedings of the ASME 2012 5th Annual Dynamic Systems and Control Conference joint with the JSME 2012 11th Motion and Vibration Conference*, **2**: 187–193, 2012, https://doi.org/10.1115/DSCC2012-MOVIC2012-8680.

13. Iooss G., Joseph D., *Elementary Stability and Bifurcation Theory*, 2nd ed., Springer, New York, 2012, https://doi.org/10.1007/978-1-4612-0997-3.

14. Jaya A.S., Kartidjo M.W., Thrust and efficiency enhancement scheme of the fin propulsion of the biomimetic autonomous underwater vehicle model in low-speed flow regime, *Ocean Engineering*, **243**: 110090, 2022, https://doi.org/10.1016/j.oceaneng.2021.110090.

15. Li G., Liu G., Leng D., Fang X., Li G., Wang W., Underwater undulating propulsion biomimetic robots: A review, *Biomimetics*, **8**(3): 318, 2023, https://doi.org/10.3390/biomimetics8030318.

16. Li J., Li W., Liu Q., Luo B., Cui W., Current status and technical challenges in the development of biomimetic robotic fish-type submersible, *Ocean-Land-Atmosphere Research*, **3**: 0036, 2024, https://doi.org/10.34133/olar.0036.

17. Li J., Ma L., Chen D., Qi Y., Bai T., Pan G., Comparative study of hydrodynamic performance of submerged water jet propeller and conventional propeller under multiple operating conditions, *Machines*, **13**(2): 147, 2025, https://doi.org/10.3390/machines13020147.

18. Li Y., Xu Y., Wu Z., Ma L., Guo M., Li Z., Li Y., A comprehensive review on fish-inspired robots, *International Journal of Advanced Robotic Systems*, **19**(3): 17298806221103707, 2022, https://doi.org/10.1177/17298806221103707.

19. Liang J., Wang T., Wen L., Development of a two-joint robotic fish for real-world exploration, *Journal of Field Robotics*, **28**(1): 70–79, 2011, https://doi.org/10.1002/rob.20363.

20. Lighthill J., Aquatic animal locomotion, [in:] *Proceedings of the 13th International Congress of Theoretical and Applied Mechanics*, Becker E., Mikhailov G.K. [Eds], pp. 29–46, Springer, Berlin, Heidelberg, 1973, https://doi.org/10.1007/978-3-642-65590-6_3.

21. Lighthill M.J., Note on the swimming of slender fish, *Journal of Fluid Mechanics*, **9**(2): 305–317, 1960, https://doi.org/10.1017/S0022112060001110.

22. Lighthill M.J., Aquatic animal propulsion of high hydromechanical efficiency, *Journal of Fluid Mechanics*, **44**(2): 265–301, 1970, https://doi.org/10.1017/S0022112070001830.

23. Lighthill M.J., Large-amplitude elongated-body theory of fish locomotion, *Proceedings of the Royal Society of London. Series B. Biological Sciences*, **179**(1055): 125–138, 1971, https://doi.org/10.1098/rspb.1971.0085.

24. Liu T., Qiu J., Geng H., Cai Y., Wang Z., Tao J., Underwater radiated noise characteristics: A comparative study of immersed and traditional waterjet propulsion systems, *Science Progress*, **108**(2): 00368504251336888, 2025, https://doi.org/10.1177/00368504251336888.

25. Maertens A., Triantafyllou M.S., Yue D.K., Efficiency of fish propulsion, *Bioinspiration & Biomimetics*, **10**(4): 046013, 2015, https://doi.org/10.1088/1748-3190/10/4/046013.

26. Mason R., Burdick J., Experiments in carangiform robotic fish locomotion, [in:] *Proceedings 2000 ICRA. Millennium Conference. IEEE International Conference on Robotics and Automation. Symposia Proceedings (Cat. No.00CH37065)*, **1**: 428–435, 2000, https://doi.org/10.1109/ROBOT.2000.844093.

27. Masoomi S.F., Gutschmidt S., Gaume N., Guillaume T., Eatwel C., Chen X., Sellier M., Design and construction of a specialised biomimetic robot in multiple swimming gaits, *International Journal of Advanced Robotic Systems*, **12**(11): 168, 2015, https://doi.org/10.5772/60547.

28. Neira J., Sequeiros C., Huamani R., Machaca E., Fonseca P., Nina W., Review on unmanned underwater robotics, structure designs, materials, sensors, actuators, and navigation control, *Journal of Robotics*, **2021**(1): 5542920, 2021, https://doi.org/10.1155/2021/5542920.

29. Omelyanyuk M., Ukolov A., Pakhlyan I., Bukharin N., El Hassan M., Experimental and numerical study of cavitation number limitations for hydrodynamic cavitation inception prediction, *Fluids*, **7**(6): 198, 2022, https://doi.org/10.3390/fluids7060198.

30. Paidoussis M.P., Hydroelastic ichthyoid propulsion, *Journal of Hydronautics*, **10**(1): 30–32, 1976, https://doi.org/10.2514/3.63050.

31. Paidoussis M.P., *Fluid-Structure Interactions: Slender Structures and Axial Flow*, vol. 1, ed. 2, Academic Press, UK, 2014.

32. Paidoussis M.P., *Fluid-Structure Interactions: Slender Structures and Axial Flow*, vol. 2, ed. 2, Academic Press, UK, 2016.

33. Petritoli E., Leccese F., Autonomous underwater glider: A comprehensive review, *Drones*, **9**(1): 21, 2025, https://doi.org/10.3390/drones9010021.

34. Schouveiler L., Chermette F., Flutter instability of freely hanging articulated pipes conveying fluid, *Physics of Fluids*, **30**(3): 034105, 2018, https://doi.org/10.1063/1.5021160.

35. Sfakiotakis M., Lane D., Davies J., Review of fish swimming modes for aquatic locomotion, *IEEE Journal of Oceanic Engineering*, **24**(2): 237–252, 1999, https://doi.org/10.1109/48.757275.

36. Smits A.J., Undulatory and oscillatory swimming, *Journal of Fluid Mechanics*, **874**: P1, 2019, https://doi.org/10.1017/jfm.2019.284.

37. Strefling P.C., Hellum A.M., Mukherjee R., Modeling, simulation, and performance of a synergistically propelled ichthyoid, *IEEE/ASME Transactions on Mechatronics*, **17**(1): 36–45, 2011, https://doi.org/10.1109/IROS.2011.6094934.

38. Struebig K., Bayat B., Eckert P., Looijestijn A., Lueth T.C., Ijspeert A.J., Design and development of the efficient anguilliform swimming robot – MAR, *Bioinspiration & Biomimetics*, **15**(3): 035001, 2020, https://doi.org/10.1088/1748-3190/ab6be0.

39. Sugiyama Y., Noda T., Studies on stability of two-degree-of-freedom articulated pipes conveying fluid: Effect of an attached mass and damping, *Bulletin of JSME*, **24**(194): 1354–1362, 1981, https://doi.org/10.1299/jsme1958.24.1354.

40. Szmidt T., Dynamics of a flutter-excited articulated ichthyoid propulsor, *Meccanica*, **60**(4): 1035–1052, 2025, https://doi.org/10.1007/s11012-025-01974-8.

41. Szmidt T., Przybyłowicz P., Critical load and non-linear dynamics of Beck's column with electromagnetic actuators, *International Journal of Non-Linear Mechanics*, **67**: 63–73, 2014, https://doi.org/10.1016/j.ijnonlinmec.2014.08.002.

42. Triantafyllou M.S., Triantafyllou G.S., An efficient swimming machine, *Scientific American*, **272**(3): 64–70, 1995, http://www.jstor.org/stable/24980373.

43. Videler J.J., *Fish swimming*, Springer, Dordrecht, 1993, https://doi.org/10.1007/978-94-011-1580-3.

44. Yu J., Wang L., Parameter optimization of simplified propulsive model for biomimetic robot fish, [in:] *Proceedings of the 2005 IEEE International Conference on Robotics and Automation*, pp. 3306–3311, IEEE, 2005, https://doi.org/10.1109/ROBOT.2005.1570620.

45. Zhong Y., Li Z., Du R., A novel robot fish with wire-driven active body and compliant tail, *IEEE/ASME Transactions on Mechatronics*, **22**(4): 1633–1643, 2017, https://doi.org/10.1109/TMECH.2017.2712820.

46. Zhou J., Si Y., Chen Y., A review of subsea AUV technology, *Journal of Marine Science and Engineering*, **11**(6): 1119, 2023, https://doi.org/10.3390/jmse11061119.

Received June 17, 2025; accepted version July 31, 2025.
Online first October 16, 2025.